

Flare Ribbons Approach Observed by the *Interface Region Imaging Spectrograph* and the *Solar Dynamics Observatory*

Ting Li^{1,2}, Jun Zhang^{1,2} & Yijun Hou^{1,2}

ABSTRACT

We report flare ribbons approach (FRA) during a multiple-ribbon M-class flare on 2015 November 4 in NOAA AR 12443, obtained by the *Interface Region Imaging Spectrograph* and the *Solar Dynamics Observatory*. The flare consisted of a pair of main ribbons and two pairs of secondary ribbons. The two pairs of secondary ribbons were formed later than the appearance of main ribbons, with respective time delays of 15 and 19 minutes. The negative-polarity main ribbon spread outward faster than the first secondary ribbon with the same polarity in front of it, and thus the FRA was generated. Just before their encounter, the main ribbon was darkening drastically and its intensity decreased by about 70 % in 2 minutes, implying the suppression of main-phase reconnection that produced two main ribbons. The FRA caused the deflection of the main ribbon to the direction of secondary ribbon with a deflection angle of about 60°. Post-approach arcade was formed about 2 minutes later and the downflows were detected along the new arcade with velocities of 35–40 km s⁻¹, indicative of the magnetic restructuring during the process of FRA. We suggest that there are three topological domains with footpoints outlined by the three pairs of ribbons. Close proximity of these domains leads to deflection of the ribbons in agreement with the magnetic field topology.

Subject headings: Sun: activity—Sun: flares—Sun: transition region— Sun: UV radiation

1. Introduction

Solar flares are among the most intense manifestations of energy release on the Sun. The magnetic reconnection process in the corona produces accelerated particles, which flow down

¹Key Laboratory of Solar Activity, National Astronomical Observatories, Chinese Academy of Sciences, Beijing 100012, China; liting@nao.cas.cn

²University of Chinese Academy of Sciences, Beijing 100049, China

along the reconnected field lines and generate flare ribbons in the lower solar atmosphere. The intersection of newly reconnected field lines with the chromosphere and transition region corresponds to flare ribbons observed in $H\alpha$ and ultraviolet (UV) wavelengths (Forbes et al. 2006; Shibata & Magara 2011). The shape, location and dynamics of flare ribbons, as well as their relationship to magnetic fields provide a significant amount of information about the three-dimensional (3D) magnetic configuration involved in the reconnection process (Gorbachev et al. 1988; Savcheva et al. 2015).

Flare ribbons are widely observed to spread systematically outwards from the polarity inversion line (PIL), which is explained by the ascending reconnection site (Fletcher et al. 2011; Schmieder et al. 2015). Moreover, flare ribbons also exhibit the apparent elongation motion along the PIL with the maximum apparent speed comparable to the local Alfvén speed (Qiu 2009; Li & Zhang 2009; Pontin et al. 2016; Priest & Longcope 2017). Sometimes unidirectional brightening propagation of two flare ribbons parallel to the PIL is associated with an asymmetric filament eruption, that is the “zipper” motion (Tripathi et al. 2006; Liu et al. 2009). Different from the zipping brightening motion, flare ribbons are also observed to move in opposite directions parallel to the PIL (Su et al. 2007; Li & Zhang 2014). Qiu et al. (2010, 2017) suggested that a large magnetic guide field parallel to the reconnection electric field may be present during the elongation motion of flare ribbons. Priest & Démoulin (1995), Masson et al. (2009) and Aulanier et al. (2006) proposed that 3D slipping magnetic reconnection at a null point, separator or quasi-separatrix layers (QSLs) can account for the elongation motion. Recently, the apparent slipping motions of flare loops and ribbons during eruptive flares were investigated by Li & Zhang (2014, 2015) and Dudík et al. (2014, 2016). The slippage exhibited a quasi-periodic pattern with a period of 3–6 minutes and its speed reached several tens of km s^{-1} .

The theoretical models usually assume a very simple magnetic field structure and generate two approximately parallel ribbons (e.g., standard flare model in the review of Shibata & Magara 2011; sheared arcade model in Somov et al. 2002). However, eruptive flares generally occur in complicated multipolar active regions (ARs) and display a three or multiple ribbon structure (Liu et al. 2015; Bamba et al. 2017). Wang et al. (2014) reported two successive eruptive flares with three ribbons parallel to the PIL and suggested that magnetic reconnection in a fan–spine magnetic topology produced the complicated ribbons. Multiple-ribbon flares consists of two parallel ribbons and several other secondary ribbons far from the center of the AR (Mandrini et al. 2006; Zheng et al. 2015, 2016). Zhang et al. (2014) found that more than a half of X-class flares in the 24th solar cycle were associated with secondary ribbons and suggested multiple sets of magnetic loops were involved in the reconnection process (Chandra et al. 2009). Direct magnetic connections between secondary ribbons and the main flare could be responsible for the brightening of the secondary ribbons.

These connections are either by magnetic loops (Herant et al. 1989; Maia et al. 2003) or by a system of null points, separatrices, and QSLs at high altitude (Schrijver & Title 2011). The brightness enhancement of secondary ribbons is generally weaker than the main central flare ribbons and appears later than the main ribbons (Zhang et al. 2014; Schmieder et al. 2015).

The observations with high temporal and spatial resolutions from the *Interface Region Imaging Spectrograph* (*IRIS*; De Pontieu et al. 2014) allow an assessment of the low atmospheric structure in unprecedented detail. In this paper, we report a multiple-ribbon flare with GOES-class M3.7 in the flare productive NOAA AR 12443 on 2015 November 4. Two pairs of secondary ribbons are successively formed after the appearance of main ribbons and the approach between one main ribbon and a secondary ribbon residing at the same magnetic polarity is firstly presented. To our knowledge, the observations of flare ribbons approach (FRA) have never been reported before. We will investigate the dynamic evolution and magnetic connectivity of multiple ribbons, and focus on the details and physical process of the FRA.

2. Observations and Data Analysis

We combine data from the *Solar Dynamics Observatory* (*SDO*; Pesnell et al. 2012) and the *IRIS* to investigate the multiple-ribbon flare and the process of FRA. The Atmospheric Imaging Assembly (AIA; Lemen et al. 2012) on board the *SDO* provides multi-filter, near-simultaneous full-Sun images with a resolution of $\sim 0''.6$ per pixel and a cadence of 12 seconds. The observations of AIA 1600, 304, 171 and 131 Å channels are used in this work. The relations of flare ribbons with magnetic fields are also studied by using the full-disk line-of-sight (LOS) magnetograms from the Helioseismic and Magnetic Imager (HMI; Scherrer et al. 2012). We concentrate on the *IRIS* slit-jaw images (SJIs) of 1400 Å with a high spatial sampling of $\sim 0''.33$ per pixel and a cadence of about 12 seconds. The field-of-view (FOV) of the SJIs covers the central part of the flaring region, and the process of FRA can be well detected. The SJI 1400 Å images are dominated by Si IV line emission from the transition region and continuum emission from the low chromosphere (Tian et al. 2014). The *IRIS* slit crosses the newly formed arcade during the approach process in a large, coarse, 16-step raster covering a FOV of $30'' \times 119''$ in 50 s with $2''$ step size. Each raster step takes about 3 s, and the spectral sampling is ~ 0.05 Å per pixel. The *IRIS* spectra of the Si IV $\lambda 1402.77$ line were analyzed and fitted by a single-Gaussian function to obtain the Doppler shifts along the arcade (Peter et al. 2014).

3. Results

3.1. Flux Rope Eruptions and Evolution of Multiple Ribbons

The analyzed M3.7 flare on 2015 November 4 was initiated at 13:31 UT and peaked at 13:52 UT from the GOES SXR 1–8 Å flux data (Figure 4(a)). About 10 minutes before the flare started, a filament at the north of AR 12443 was activated and showed an evident clockwise rotation around the filament axis (Figure 1(a); see Animation 304-eruption). The filament gradually developed into two filament structures F1 and F2 as seen from the 304 Å images (Figure 1(b)). Then the filament materials of F1 and F2 moved in opposite directions from their crossing location (white arrows in Figure 1(b)), implying the occurrence of tether-cutting reconnection (Moore et al. 2001; Chen et al. 2016). We obtained the stack plots along the moving directions of filament materials and then calculated the bidirectional velocities of about 150 km s^{-1} and 210 km s^{-1} for F1 and F2. Meanwhile, two quasi-parallel flare ribbons R1 and R2 appeared underlying the eruptive filament F1. Starting from 13:32 UT, R2 at the east appeared and propagated to southeast at a speed of about 120 km s^{-1} (green arrows in Figures 1 (c)-(d)), which finally formed a hook-shaped segment with a length of about 80 Mm. In the high-temperature channel of 131 Å (about 11 MK), two flux ropes FR1 and FR2 were detected (Figures 1 (e)-(f); see Animation 131-eruption), with their lower parts corresponding to the two filaments F1 and F2 (Li & Zhang 2013; Cheng et al. 2014). The flux rope FR1 exhibited an asymmetric eruption with its eastern footpoints slipping along the hook of R2 (Figures 1 (g)-(h)) and finally delineated a “triangle-shaped flag” surface. The observations are similar to the event presented by Li & Zhang (2014) and imply the occurrence of slipping magnetic reconnection. R1 resided at negative-polarity magnetic fields and R2 at positive-polarity fields (Figure 1(e)).

About 15 minutes after the flare onset ($\sim 13:46 \text{ UT}$), a pair of secondary ribbons PSR1 and NSR1 appeared adjacent to two main ribbons R1 and R2 (Figures 2(a)-(b)). Later on, the interaction between ribbons R1 and NSR1 was initiated when R1 chased up NSR1 (Figure 2(c)). The detailed analysis of the approach process is carried out in Figures 3-5. The west cusp of ribbon R2 extended to the north and encountered the ribbon PSR1 (green arrows in Figure 2(c)-(d)). Then R2 and PSR1 approached each other and a brightening between the R2 and PSR1 ribbons was observed (see 13:50 UT in Animation 304-eruption). Afterwards the brightening propagated to the north along the hook-shaped segment of R2. Another pair of secondary ribbons PSR2 and NSR2 were detected about 4 minutes after the appearance of PSR1 and NSR1 (Figure 2(c)). Afterwards, the intensities and widths of PSR2 and NSR2 were both increased at 13:56 UT (Figure 2(d)). The 131 Å observations showed the existence of hot coronal loops connecting PSR1 and NSR1 (Figures 2(f)-(g)), indicative of their conjugated property. Similarly, the high-temperature loops connecting

PSR2 and NSR2 can also be detected (red dotted curves in Figure 2(h)).

The overlay of the flare ribbon time evolution over the magnetogram is displayed in Figure 2(e). The color indicates the time of the ribbon brightness observed at *SDO* 1600 Å and *IRIS* 1400 Å. The west ribbons NSR1 and NSR2 anchored at the negative-polarity magnetic fields and the east ones at the positive-polarity fields. It shows that the generally parallel portions of two main ribbons R1 and R2 exhibit an evident separation motion with the high-temperature flare loops connecting them. Two pairs of secondary ribbons are formed later than the main ribbons. Each pair of secondary ribbons has corresponding coronal loops that appear right after the formation of these ribbons. We suggest that there are three topological domains with footpoints outlined by the three pairs of ribbons. The approach process of ribbons R1 and NSR1 is interpreted as the interaction of two different topological domains.

3.2. Approach Process Between Two Ribbons

The ribbons R1, NSR1 and NSR2 at the west were clearly observed by the *IRIS*, and thus the details of flare ribbon interactions can be well obtained. The main ribbon R1 continually spread towards the southwest as the flare developed (Figures 3(a)-(c); see Animation 1400-approach). At 13:46 UT, the secondary ribbon NSR1 was formed in front of R1 and was composed of numerous slipping dot-like substructures (Figure 3(b)). Later on, the arch-shaped ribbon NSR1 moved southward with a smaller speed than R1, resulting in the distance between NSR1 and R1 becoming smaller and smaller. About 4 minutes later, another secondary ribbon NSR2 appeared at the south of NSR1 (Figure 3(c)). Then the three ribbons R1, NSR1 and NSR2 kept moving to the south. Starting from 13:51 UT, the ribbon R1 was darkening with the intensity decrease of about 70 % when R1 moved close to NSR1 (Figure 3(d)). From then on, the ribbon R1 continually approached to NSR1 and evident brightening appeared at the merging location (Figure 3(e)). From about 13:55 UT, the brightening at the west was detected to propagate from the interaction location to the west (black arrows in Figures 3(f)-(h)). The direction of brightening propagation was almost consistent with NSR1 (Figure 3(i)). After examining the 1400 Å data, we suggest that the newly formed brightening could be associated with the evolving ribbon R1 deflected by the NSR1 ribbon by about 60° (see Figure 3(i)).

The spatio-temporal relations among the three ribbons R1, NSR1 and NSR2 were presented in Figure 4. The propagating velocity of R1 decreased from 13.1 km s⁻¹ at 13:38 UT to 4.8 km s⁻¹ at 13:51 UT just before the approach (Figure 4(b)). About 15 minutes after the flare started, NSR1 appeared and propagated southward at a speed of about 1.5 km s⁻¹

(Figure 4(a)). NSR2 was formed about 19 minutes after the flare onset and moved in front of NSR1 at a velocity of 4.3 km s^{-1} . Then evident darkening process of R1 was started at about 13:51 UT when R1 and NSR1 were very close to each other (distance of 1.2 Mm) and the intensity decreased by 70 % in 2 minutes (Figure 4(b)). The FRA of R1 and NSR1 were initiated at 13:53 UT (blue dash-dotted lines in Figure 4) and caused the brightening at the interaction location. Afterwards, the ribbon R1 was deflected to the direction of NSR1. As seen from the stack plot (Figure 4(c)) along slice “C–D” (blue line in Figure 3(f)), there were two times of propagations of deflected R1 with their velocities reaching about 71 and 54 km s^{-1} .

Associated with the FRA, part of the arcade was newly formed at the northeast of the interaction location from about 13:55 UT (Figures 5(a) and (d)). Then the mass flows from the top of the arcade to its two ends appeared and a large part of the arcade could be detected in 171 Å and 1400 Å channels (Figures 5(b) and (e)). The east end of the arcade was located at the positive-polarity fields and the west end anchored in the negative-polarity fields (contours in Figure 5(b)). The top part of the arcade could also be observed at 1600 Å (Figure 5(c)), implying the lower-temperature component of the arcade. At about 13:59 UT, the arcade became more extended and its west leg was connected with the deflected R1 (Figure 5(f)). By plotting the space-time map of 1400 Å (Figure 5(g)) along slice “E–F” (Figure 5(f)), we have inferred the speeds of downflows with values of 35 and 40 km s^{-1} . As seen from the space-time map, the arcade was formed about 2 minutes later than the initiation of FRA (blue and white dash dotted lines), and thus we name the newly formed arcade as post-approach arcade (PAA). The spectra of Si IV $\lambda 1402.77$ line at three different locations (diamonds in Figures 5(e)-(f)) of PAA were displayed in Figures 5(h)-(i). At 13:57 UT, two east locations showed blueshifts of about 9 and 12 km s^{-1} while the west location exhibited a redshift of 5 km s^{-1} (Figure 5(h)). About 2 minutes later, the blueshifts at two east locations reached about 13 and 11 km s^{-1} and the redshift at the west leg increased to 8 km s^{-1} (Figure 5(i)).

4. Summary and Discussion

We present the *IRIS* and *SDO* observations of the approach process between one main ribbon R1 and a secondary ribbon NSR1 with the same magnetic polarity during a multiple-ribbon M3.7 flare on 2015 November 4. The two main ribbons of the flare had a portion generally parallel to each other and also a hook-shaped segment at the east of the positive-polarity ribbon, which propagated towards the southeast at a speed of about 120 km s^{-1} . Meanwhile the east footpoints of the associated flux rope displayed a slipping motion along

the hook, delineating a “triangle-shaped flag surface”. Two pairs of secondary ribbons were formed successively at the periphery of two main ribbons in the late stage of the impulsive phase. R1 spread outward much faster than NSR1 in front of it and the distance between the two ribbons became smaller and smaller. R1 began to darken evidently and its intensity decreased by 70 % in 2 minutes when it came very close to NSR1 (less than 1.2 Mm). Then R1 approached to NSR1 and caused the deflection of ribbon R1 with a deflection angle of about 60° . The deflected R1 propagated in the direction of NSR1 at velocities of 50–70 km s^{-1} . A new loop structure PAA was formed during the FRA, with its west leg connecting with the deflected R1. The downflows along the PAA had Doppler shifts of about 10 km s^{-1} and projected velocities of 40 km s^{-1} in the plan of sky.

The secondary ribbons were formed in pairs and sequentially at the periphery of main ribbons after the flare onset, with respective time delays of 15 and 19 minutes for the first and second pairs of secondary ribbons. The conjugate footpoints of each pair of secondary ribbons were connected by high-temperature coronal loops. Previous studies suggested that the initial magnetic reconnections in main flare regions triggered the high-latitude null-point reconnections in a fan-spine-like topology (Joshi et al. 2015; Liu et al. 2015) or long-distance loop-loop interactions (Maia et al. 2003; Chandra et al. 2009) and thus produced the secondary ribbons. The secondary ribbons in our observations were composed of numerous small-scale slipping substructures, which correspond to the footpoints of reconnected field lines (Li & Zhang 2015). We suggest that the flux rope eruption pushes overlying loops against the neighboring topological domain and then magnetic reconnections between the erupting domain and its neighboring one result in the formation of the first pair of secondary ribbons. Later on, another topological domain is disturbed after the appearance of ribbons PSR1 and NSR1 and generates the second pair of secondary ribbons.

Associated with the FRA of ribbons R1 and NSR1, several new observational features have been identified. The ribbons R1 and NSR1 corresponded to the ends of reconnected magnetic lines in two different topological domains (Fletcher et al. 2011; Schmieder et al. 2015). Associated with the separation motion of two main ribbons, magnetic reconnection in the center region was gradually spreading towards the border of the topological domain. When magnetic reconnection occurred at the border of the topological domain, it encountered with another neighboring topological domain and resulted in the phenomenon of FRA. We suggest that the interaction location corresponded to the boundary of two different domains. The close proximity of these domains caused the deflection of ribbon R1 with a deflection angle of about 60° . The deflected ribbon propagated in the direction consistent with NSR1, in agreement with the magnetic topology of the neighboring domain. The rapid “darkening” of R1 just before the approach implied that coronal magnetic reconnection was suppressed at the boundary of different magnetic systems. Furthermore, the newly formed

loop structure PAA indicated that magnetic restructuring was involved in the process of FRA. The downflows along the PAA were simultaneously detected based on the imaging and spectral observations, which probably corresponded to reconnection downflows. However, the triggering mechanism of secondary ribbons and physical process of FRA are still open questions. In the future, more observational and simulation studies are required to understand the process of FRA as well as other complicated dynamic evolution of solar flares.

We are grateful to Kai Yang and Shu-Hong Yang for useful discussions. *SDO* is a mission of NASA's Living With a Star Program. *IRIS* is a NASA small explorer mission developed and operated by LMSAL with mission operations executed at NASA's Ames Research center and major contributions to downlink communications funded by the Norwegian Space Center (NSC, Norway) through an ESA PRODEX contract. This work is supported by the National Natural Science Foundations of China (11773039, 11533008, 11673035 and 11673034) and the Youth Innovation Promotion Association of CAS (2017078).

REFERENCES

- Aulanier, G., Pariat, E., Démoulin, P., & DeVore, C. R. 2006, *Sol. Phys.*, 238, 347
- Bamba, Y., Inoue, S., Kusano, K., & Shiota, D. 2017, *ApJ*, 838, 134
- Chandra, R., Schmieder, B., Aulanier, G., & Malherbe, J. M. 2009, *Sol. Phys.*, 258, 53
- Chen, H., Zhang, J., Li, L., & Ma, S. 2016, *ApJ*, 818, L27
- Cheng, X., Ding, M. D., Zhang, J., et al. 2014, *ApJ*, 789, L35
- De Pontieu, B., Title, A. M., Lemen, J. R., et al. 2014, *Sol. Phys.*, 289, 2733
- Dudík, J., Janvier, M., Aulanier, G., et al. 2014, *ApJ*, 784, 144
- Dudík, J., Polito, V., Janvier, M., et al. 2016, *ApJ*, 823, 41
- Fletcher, L., Dennis, B. R., Hudson, H. S., et al. 2011, *Space Sci. Rev.*, 159, 19
- Forbes, T. G., Linker, J. A., Chen, J., et al. 2006, *Space Sci. Rev.*, 123, 251
- Gorbachev, V. S., Kelner, S. R., Somov, B. V., & Shvarts, A. S. 1988, *Soviet Ast.*, 32, 308
- Herant, M., Golub, L., & Neidig, D. F. 1989, *Sol. Phys.*, 124, 145

- Joshi, N. C., Liu, C., Sun, X., et al. 2015, *ApJ*, 812, 50
- Lemen, J. R., Title, A. M., Akin, D. J., et al. 2012, *Sol. Phys.*, 275, 17
- Li, L., & Zhang, J. 2009, *ApJ*, 690, 347
- Li, T., & Zhang, J. 2013, *ApJ*, 778, L29
- Li, T., & Zhang, J. 2014, *ApJ*, 791, L13
- Li, T., & Zhang, J. 2015, *ApJ*, 804, L8
- Liu, C., Deng, N., Liu, R., et al. 2015, *ApJ*, 812, L19
- Liu, R., Alexander, D., & Gilbert, H. R. 2009, *ApJ*, 691, 1079
- Maia, D., Aulanier, G., Wang, S. J., et al. 2003, *A&A*, 405, 313
- Mandrini, C. H., Demoulin, P., Schmieder, B., et al. 2006, *Sol. Phys.*, 238, 293
- Masson, S., Pariat, E., Aulanier, G., & Schrijver, C. J. 2009, *ApJ*, 700, 559
- Moore, R. L., Sterling, A. C., Hudson, H. S., & Lemen, J. R. 2001, *ApJ*, 552, 833
- Pesnell, W. D., Thompson, B. J., & Chamberlin, P. C. 2012, *Sol. Phys.*, 275, 3
- Peter, H., Tian, H., Curdt, W., et al. 2014, *Science*, 346, 1255726
- Pontin, D., Galsgaard, K., & Démoulin, P. 2016, *Sol. Phys.*, 291, 1739
- Priest, E. R., & Démoulin, P. 1995, *J. Geophys. Res.*, 100, 23443
- Priest, E. R., & Longcope, D. W. 2017, *Sol. Phys.*, 292, 25
- Qiu, J. 2009, *ApJ*, 692, 1110
- Qiu, J., Liu, W., Hill, N., & Kazachenko, M. 2010, *ApJ*, 725, 319
- Qiu, J., Longcope, D. W., Cassak, P. A., & Priest, E. R. 2017, *ApJ*, 838, 17
- Savcheva, A., Pariat, E., McKillop, S., et al. 2015, *ApJ*, 810, 96
- Scherrer, P. H., Schou, J., Bush, R. I., et al. 2012, *Sol. Phys.*, 275, 207
- Schmieder, B., Aulanier, G., & Vršnak, B. 2015, *Sol. Phys.*, 290, 3457

- Schrijver, C. J., & Title, A. M. 2011, *Journal of Geophysical Research (Space Physics)*, 116, A04108
- Shibata, K., & Magara, T. 2011, *Living Reviews in Solar Physics*, 8, 6
- Somov, B. V., Kosugi, T., Hudson, H. S., Sakao, T., & Masuda, S. 2002, *ApJ*, 579, 863
- Su, Y., Golub, L., & Van Ballegooijen, A. A. 2007, *ApJ*, 655, 606
- Tian, H., DeLuca, E., Reeves, K. K., et al. 2014, *ApJ*, 786, 137
- Tripathi, D., Isobe, H., & Mason, H. E. 2006, *A&A*, 453, 1111
- Wang, H., Liu, C., Deng, N., et al. 2014, *ApJ*, 781, L23
- Zhang, J., Li, T., & Yang, S. 2014, *ApJ*, 782, L27
- Zheng, R., Korsós, M. B., & Erdélyi, R. 2015, *ApJ*, 809, 45
- Zheng, R., Chen, Y., & Wang, B. 2016, *ApJ*, 823, 136

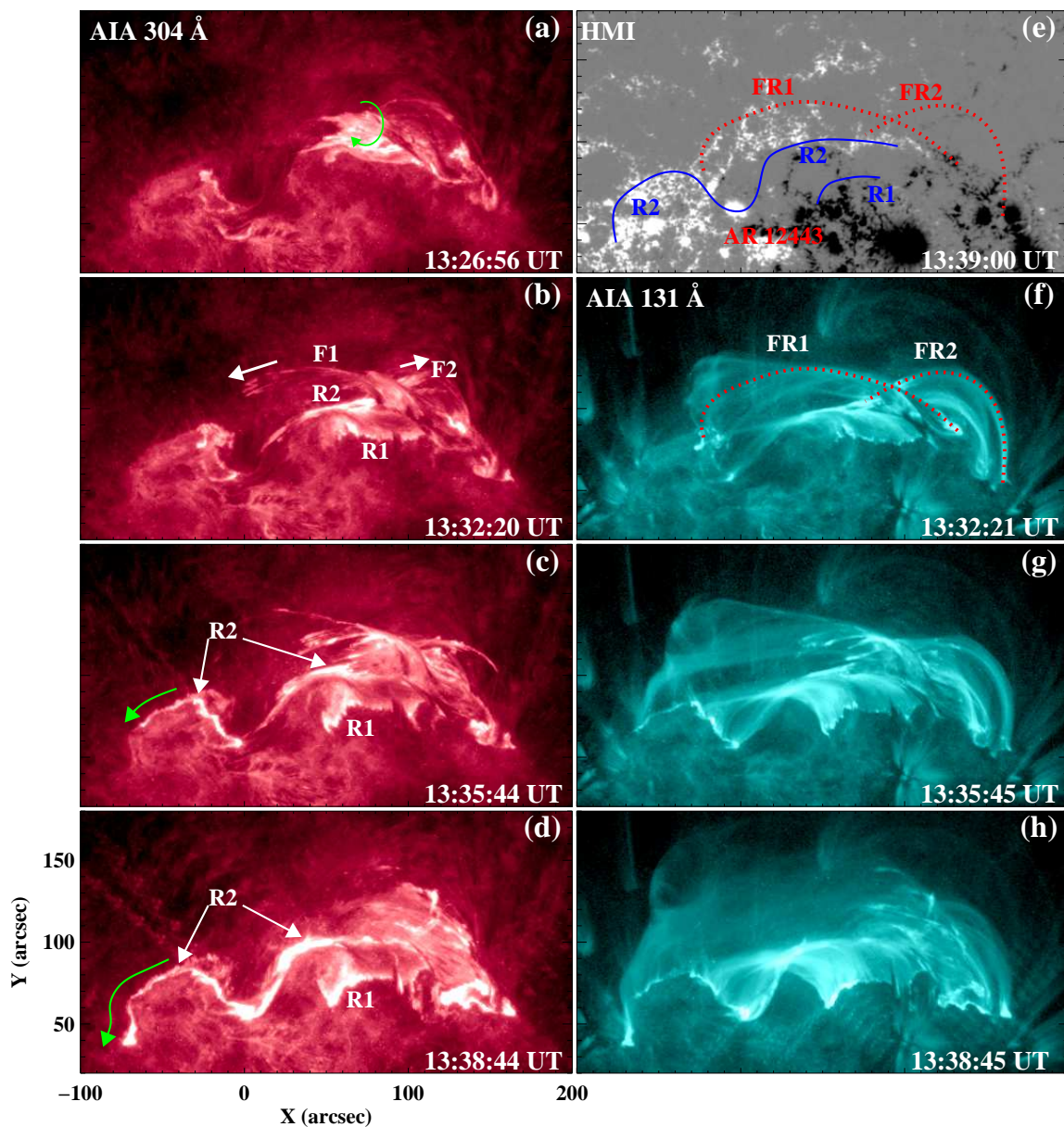


Fig. 1.— Time sequences of *SDO*/AIA 304 Å images, 131 Å images and *SDO*/HMI LOS magnetogram showing the evolution of flux ropes and the M3.7 flare in AR 12443 on 2015 November 4 (see Animations 304-eruption and 131-eruption). The green arrow in panel (a) denotes the clockwise rotation of the filament and the white arrows in panel (b) represent the bidirectional flows along two filaments F1 and F2. R1 and R2 are two main flare ribbons, and green arrows in panels (c)-(d) point to the propagating direction of the hooked segment of R2. Red dotted lines in panels (e)-(f) outline the main axes of flux ropes FR1 and FR2. Blue solid lines in panel (e) show the morphologies of ribbons R1 and R2 at 13:39 UT.

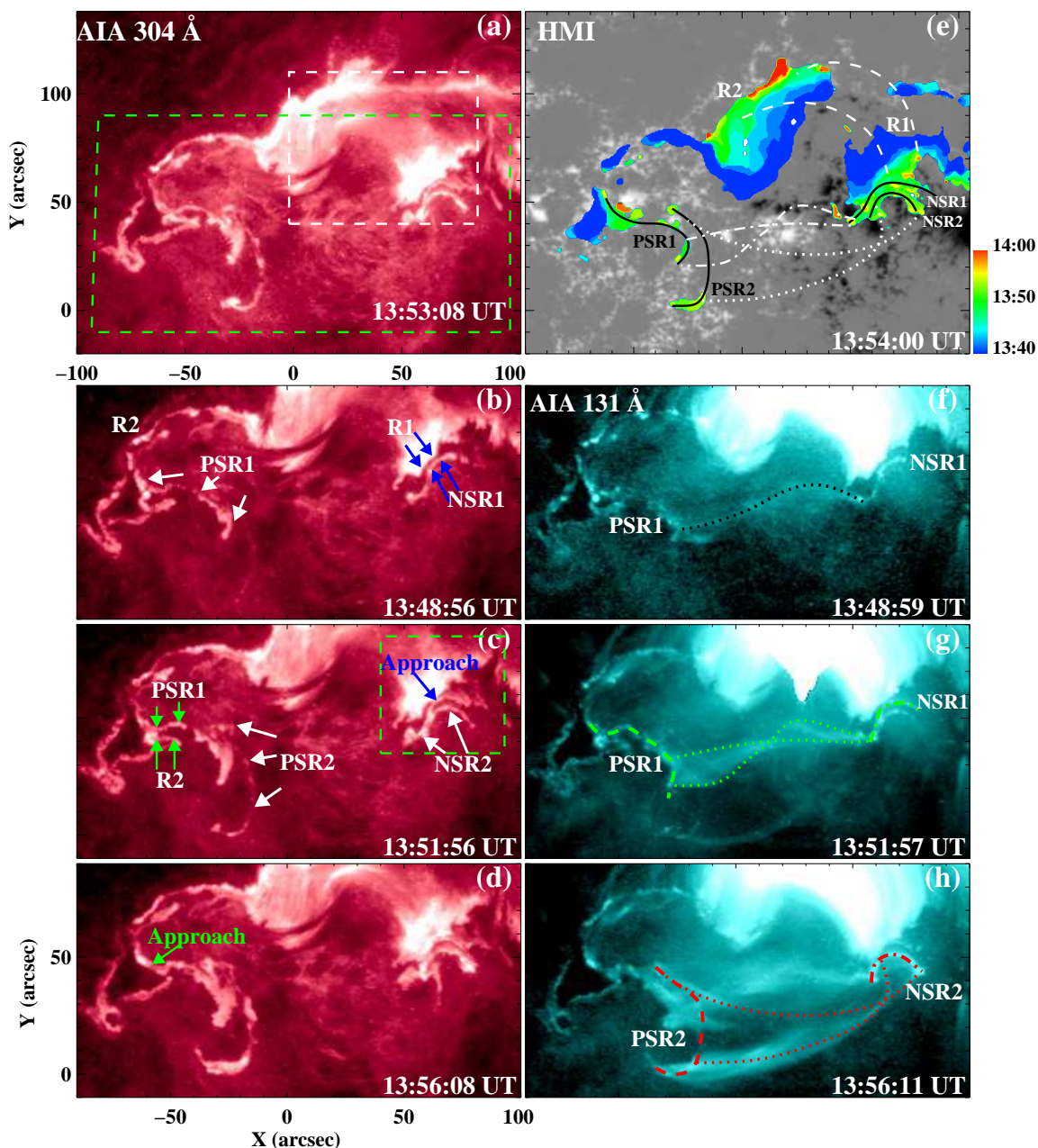


Fig. 2.— Appearance of two pairs of secondary ribbons (PSR1-NSR1, PSR2-NSR2) and their interactions with main ribbons R1 and R2 in the late phase of the flare. The green and white rectangles in panel (a) respectively denote the FOVs of the images in panels (b)-(d), panels (f)-(h) and Figure 5. The green rectangle in panel (c) shows the FOV of Figure 3. Panel (e) shows the *SDO*/HMI LOS magnetogram with an overlay of the positions of newly brightened ribbons. The color indicates the time of the ribbon brightness from 13:40 UT to 14:00 UT in the images of 1600 Å and 1400 Å. Green lines in panel (g) show the first pair of secondary ribbons PSR1 and NSR1 and high-temperature loops connecting them. Red lines in panel (h) denote the second pair of secondary ribbons PSR2 and NSR2 and their connecting loops. Their duplications are also shown in panel (e).

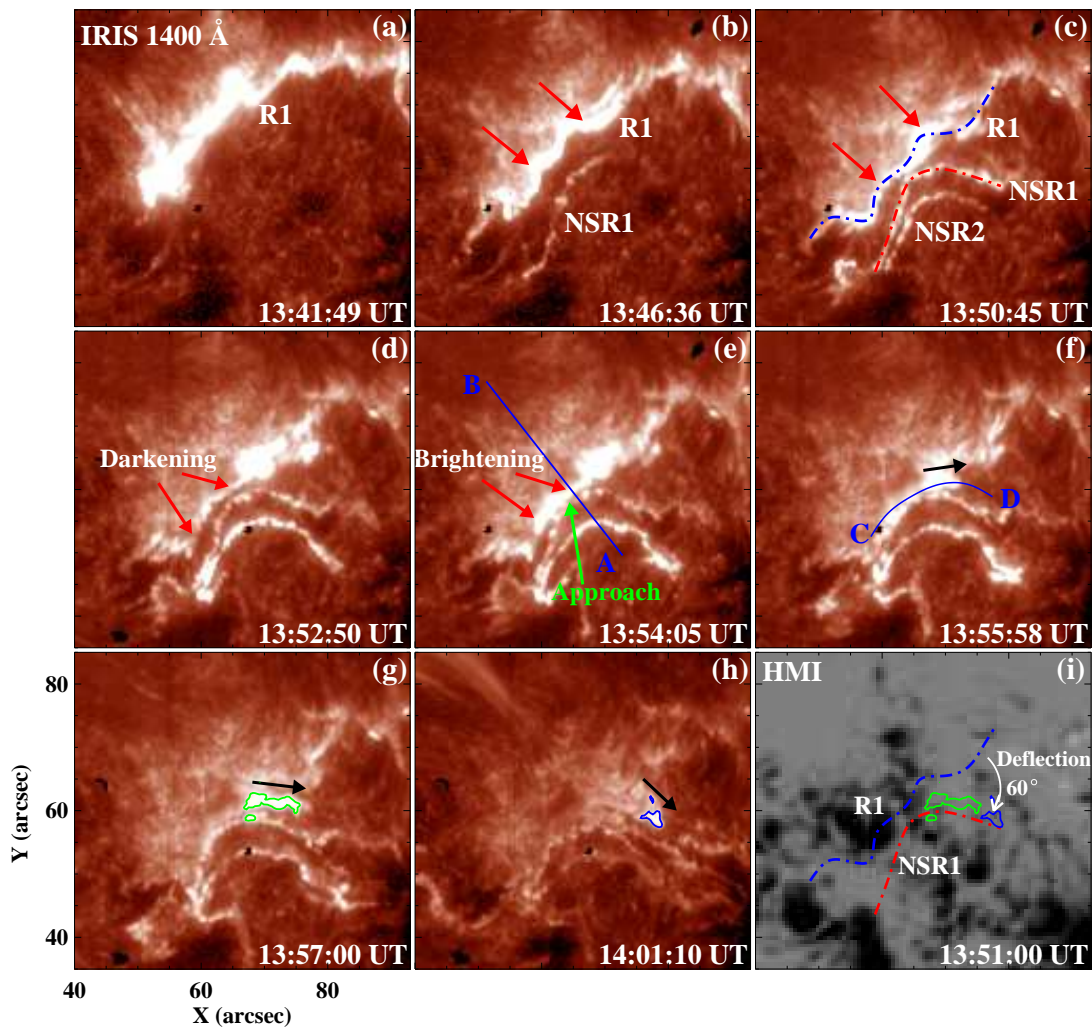


Fig. 3.— Time sequence of *IRIS* 1400 Å images and *SDO*/HMI LOS magnetogram showing the approach process between ribbons R1 and NSR1 (see Animation 1400-approach). Red arrows in panels (b)-(c) represent the propagating direction of R1. Blue and red dash-dotted lines in panel (c) outline ribbons R1 and NSR1, and are duplicated in the magnetogram of panel (i). Blue lines “A–B” and “C–D” show the cut positions used to obtain the time-distance plots shown in Figures 4(a) and (c). Black arrows in panels (f)-(h) denote the propagation of deflected ribbon after the ribbons approach (FRA) of R1 and NSR1. The green and blue curves in panels (g)-(h) are the brightness of deflected ribbon, and their duplications are also shown in panel (i).

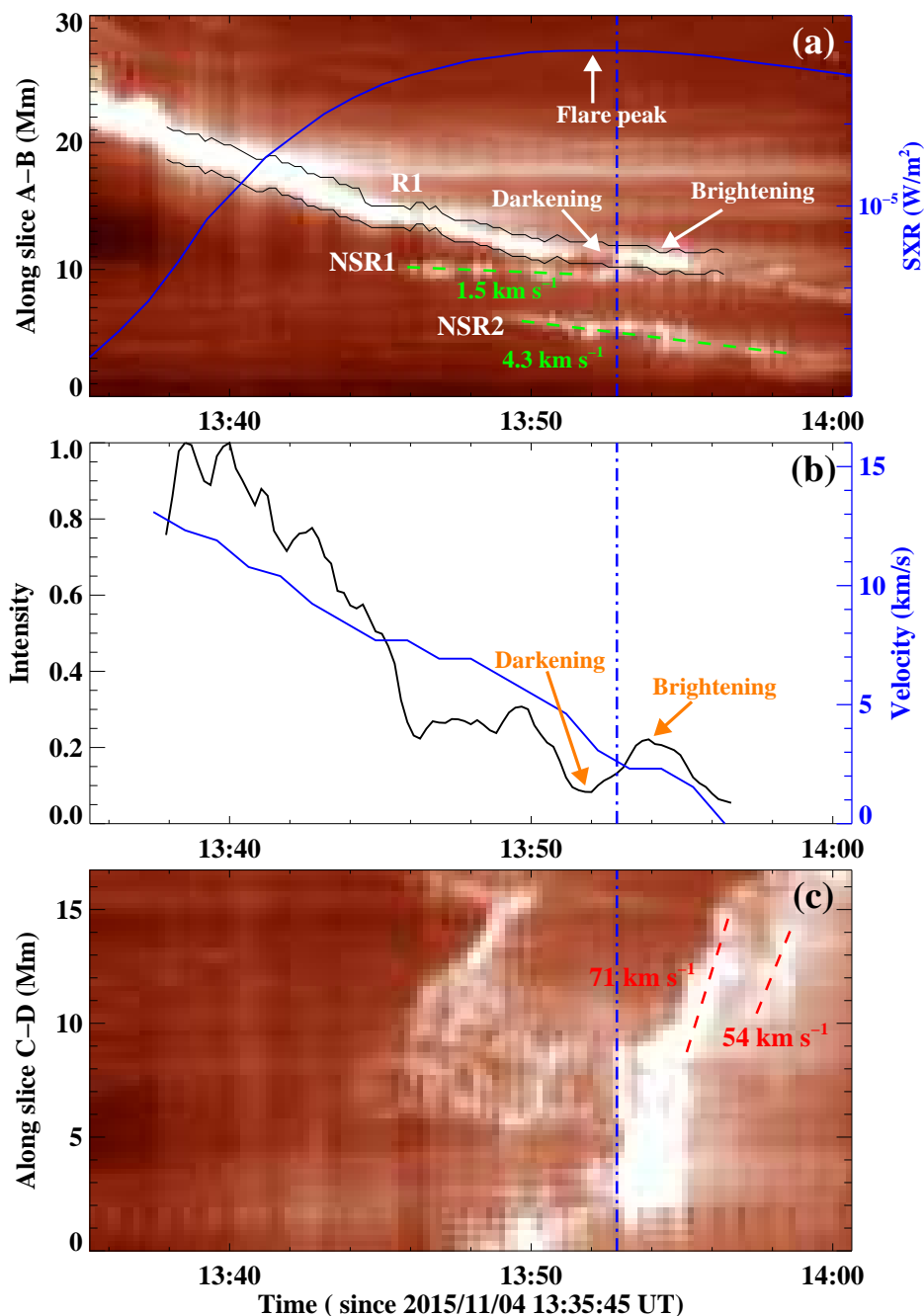


Fig. 4.— Panel (a): time-distance plot along slice “A–B” (blue line in Figure 3(e)) at 1400 \AA . The blue curve shows GOES SXR 1–8 Å flux of the M3.7 flare. Blue dash-dotted line denotes the start time of FRA between R1 and NSR1. Panel (b): evolution of intensity (black curve) and propagating velocity (blue curve) of R1. The calculated region of the intensity and velocity is within the black curves in panel (a). Panel (c): time-distance plot along slice “C–D” (blue line in Figure 3(f)). Red dashed lines outline the propagations of the deflected ribbon.

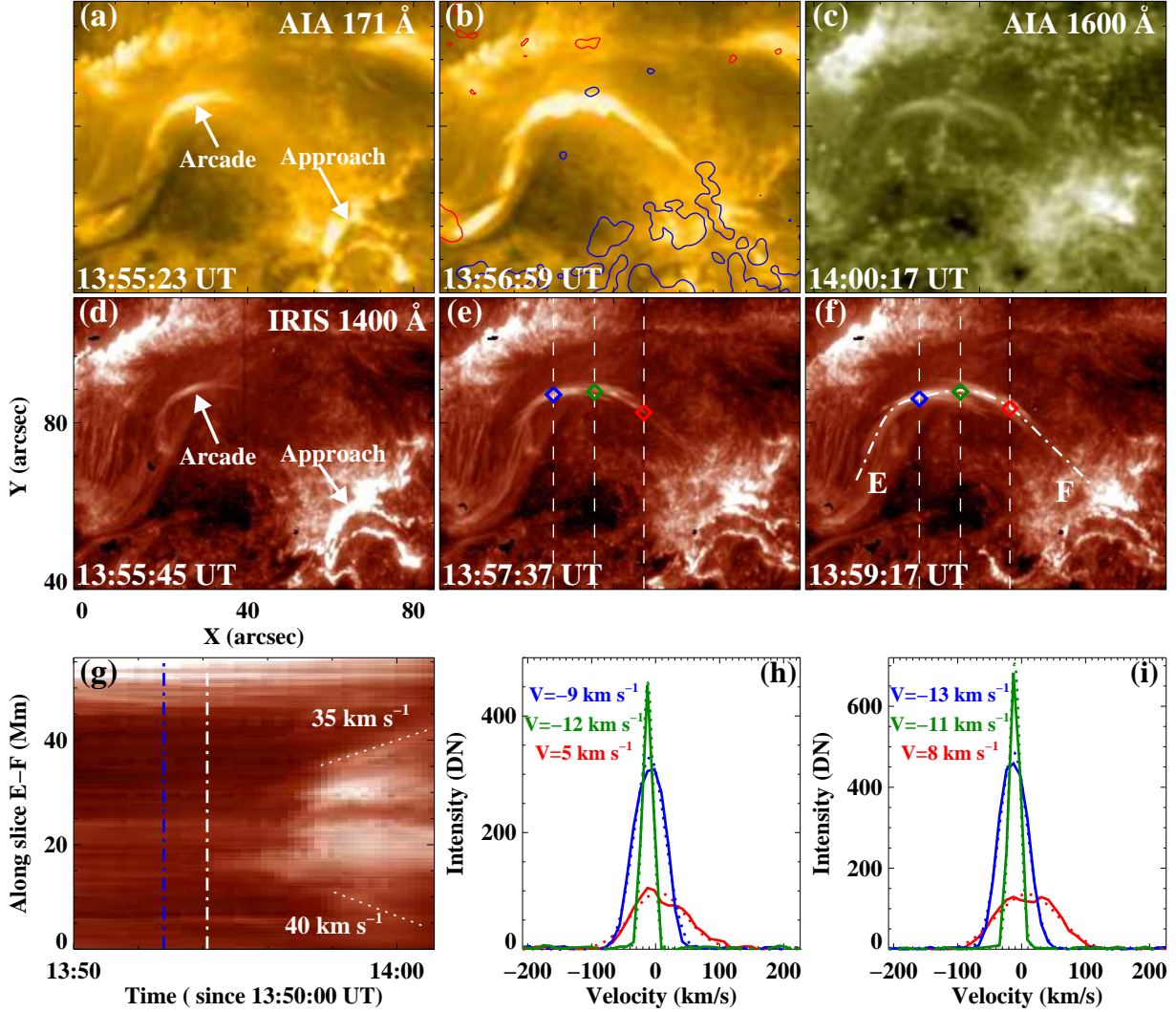


Fig. 5.— Panels (a)-(f): multi-wavelength observations of the post-approach arcade (PAA) during the approach process. The red and blue contours in panel (b) are the magnetic fields at ± 500 G levels at the ends of the PAA. Dashed lines in panels (e)-(f) show the slit locations and the diamonds denote the intersections of the PAA and the slit. Dash-dotted curve “E–F” in panel (f) shows the cut position used to obtain the time-distance plot shown in panel (g). Panel (g): time-distance plot along slice “E–F” at 1400 Å. Blue and white dash dotted lines respectively represent the start of FRA and the appearance of PAA. Panel (h): profiles of the Si IV $\lambda 1402.77$ line at different locations (diamonds in panel (e)) along the PAA. The dotted curves are the corresponding single-Gaussian fitting profiles. Panel (i): similar to panel (h) but for the diamond locations in panel (f).